



Research article

Georg Ulrich, Emanuel Pfitzner, Arne Hoehl, Jung-Wei Liao, Olga Zadvorna, Guillaume Schweicher, Henning Sirringhaus, Joachim Heberle, Bernd Kästner*, Jörg Wunderlich and Deepak Venkateshvaran

Thermoelectric nanospectroscopy for the imaging of molecular fingerprints

<https://doi.org/10.1515/nanoph-2020-0316>

Received June 4, 2020; accepted July 30, 2020; published online August 21, 2020

Abstract: We present a nanospectroscopic device platform allowing simple and spatially resolved thermoelectric detection of molecular fingerprints of soft materials. Our technique makes use of a locally generated thermal gradient converted into a thermoelectric photocurrent that is read out in the underlying device. The thermal gradient is generated by an illuminated atomic force microscope tip that localizes power absorption onto the sample surface. The detection principle is illustrated using a concept device that contains a nanostructured strip of polymethyl methacrylate (PMMA) defined by electron beam lithography. The platform's capabilities are demonstrated through a comparison between the spectrum obtained by on-chip thermoelectric nanospectroscopy with a nano-FTIR spectrum recorded by scattering-type scanning near-field optical microscopy at the same position. The subwavelength spatial resolution is demonstrated by a spectral line scan across the edge of the PMMA layer.

Keywords: nanospectroscopy; photothermoelectric effect; s-SNOM.

1 Introduction

Combining vibrational spectroscopy with atomic force microscopy (AFM) into one measurement system merges the key advantages of both techniques and offers wavelength independent chemical imaging and identification down to the nanoscale. This advanced scanning probe methodology has been implemented in tip-enhanced Raman spectroscopy (TERS) [1, 2] and infrared (IR) scattering-type scanning near-field optical microscopy (s-SNOM) [3–5] which detect light (in)elastically scattered from the AFM tip. In contrast, the implementation by photothermal-induced resonance (PTIR) imaging [6] or photoinduced force microscopy (PiFM) [7, 8] analyzes the mechanical and thermal response to IR excitation of the sample itself. A recent alternative approach termed photocurrent near-field microscopy [9–13] avoids the sophisticated s-SNOM or PTIR detection schemes by an on-chip thermoelectric detection of IR excitations. This approach simplified IR nanoimaging of propagating graphene plasmons [10] and promises on-chip spectroscopy, imaging, and sensing. Often, the material under investigation – usually graphene – acts as the detection material at the same time; however, plasmon polaritons for the purpose of analyzing graphene covering films have also been reported [14]. Recently, a device combining hyperbolic phonon-polaritons of hexagonal boron nitride propagating as a waveguide mode toward a detecting graphene *pn*-junction allowed for disentangling the two functions [15], but the geometric and dielectric requirements of such devices limit the universal application to arbitrary material systems.

In this paper, we show that a conventional ferromagnetic multilayer system can act as a thermocouple, functioning as a thermoelectric detector material to analyze the thermal response of a sample layer made of a nonconducting material on top. This allows to directly access the sample's molecular fingerprint, i.e., the spectrum by which the molecule can be identified, with subwavelength spatial resolution in a simple manner.

***Corresponding author: Bernd Kästner**, Physikalisch-Technische Bundesanstalt, Berlin, Germany, E-mail: bernd.kaestner@ptb.de, <https://orcid.org/0000-0002-6575-6621>

Georg Ulrich and Arne Hoehl, Physikalisch-Technische Bundesanstalt, Berlin, Germany. <https://orcid.org/0000-0002-0664-8698> (G. Ulrich)

Emanuel Pfitzner and Joachim Heberle, Freie Universität, Berlin, Germany

Jung-Wei Liao, University of Cambridge, Cambridge, UK; Durham Magneto Optics Ltd, Caxton, UK

Olga Zadvorna, Guillaume Schweicher, Henning Sirringhaus and Deepak Venkateshvaran, University of Cambridge, Cambridge, UK

Jörg Wunderlich, Universität Regensburg, Regensburg, Germany; Czech Academy of Sciences, Praha, Czech Republic

2 Layout

The device operates in two stages. In the first stage, the top insulating layer converts radiation power of the locally confined near-field $\mathbf{E}(\mathbf{r}, \omega)$ into heat P_h per volume unit V depending on its dielectric properties, $\varepsilon(\omega)$, according to [16, 17]

$$\frac{dP_h}{dV} = \frac{1}{2} [\omega \text{Im}(\varepsilon(\omega))] |\mathbf{E}|^2. \quad (1)$$

In the second stage, an underlying conductive thermoelectric layer acts as a *detecting* film by converting the heat flow into an electric response by means of the Seebeck effect occurring in materials of different Seebeck coefficients.

The sandwich construction of our thermoelectric sensor is depicted in Figure 1. It consists of a heterostructure of alternating CoFeB and Pt layers of 1 nm each and capped with a 4 nm protective Pt layer to avoid oxidation. The above heterostructure was grown on a buffer bilayer of Ta (2 nm)/Pt (2 nm) on a SiO₂/Si substrate. The SiO₂ layer is 500 nm thick ensuring thermal insulation to the Si wafer. The composition of the layers and the device geometry allows us to employ magnetic and nonmagnetic thermoelectric effects [12, 18, 19] (see Supplementary material). However, the nonmagnetic Seebeck contributions dominate in the current structure.

The multilayer stack, patterned into a bar by e-beam lithography and ion milling, is electrically contacted on either side by two 20 nm thick, 2 μm wide, Pt strips that overlap the heterostructure bar by 500 nm leaving a gap of 1 μm between them. As we will show below, one of the contacts serves as the detecting area where the material to be characterized will be deposited. The other contact can be used as the reference, where the spectral response is known or deliberately modified. The whole structure was grown on a thermally oxidized Si substrate to prevent thermal conduction to the substrate.

Using e-beam lithography, a 50 nm thick and 0.8 μm wide stripe of PMMA was defined along the Pt contacts. In a

subsequent step, part of the PMMA stripe was cross-linked ($\#$) on one side of the multilayer structure, while part was left pristine (\parallel) on the other side. The partition between the cross-linked and pristine PMMA regions is shown in Figure 2. It can be seen that cross-linking results in a reduced layer thickness.

The PMMA stripe will serve in the following as a spectroscopic marker exhibiting a strong absorptive band at $\approx 1730 \text{ cm}^{-1}$ only if it was not cross-linked [20]. Such prepared structures were raster-scanned by a metallized AFM tip illuminated by a quantum cascade laser (QCL) with the emission frequency tuned to 1730 cm^{-1} . Simultaneous to the acquisition of the scattered light, the generated thermovoltage is demodulated at multiples n of the tip resonance frequency $n\Omega$ with Ω typically around 250 kHz and registered for each pixel.

Higher harmonic demodulation is typically used to filter out only the near-field scattered light over light scattered at impurities on the sample or the tip shaft interfering with the near-field scattered light. In the presented device, the size of the active area is smaller than the wavelength of the incident light. This makes demodulation at higher harmonics unnecessary since the detected voltage is not corrupted by light scattered at other scatterers on the sample or the tip shaft itself. Approach curves are provided in the Supplementary material showing the near-field contributions of the signals demodulated at $n = 1$ and $n = 2$. They indicate that demodulation at the fundamental harmonic frequency is already sufficiently suppressing interfering background signals.

3 Device operation

Figure 2 shows the topography in (a), magnitudes of the induced thermovoltage demodulated at the fundamental and second harmonic of the tip frequency Ω , $|V_{\text{Th},1,2}|$ in (b) and (c), respectively, and the according phase, ϕ_2 (phase between thermovoltage and tip oscillation) in (d). The thermovoltage is only generated in the areas close to

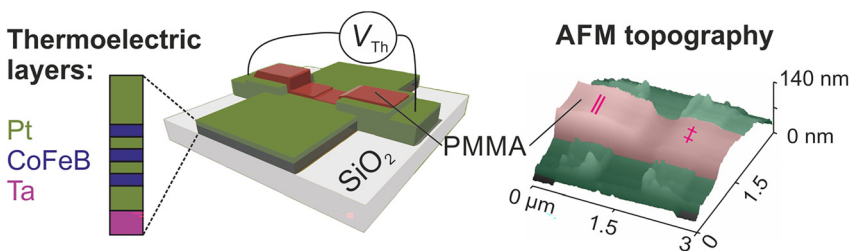


Figure 1: Schematic of the device, a heterostructure of CoFeB (blue) and Pt (green). The polymethyl methacrylate (PMMA) layer to be detected is shown in brown. Details on the layer thicknesses are provided in the main text. A false-color atomic force microscopy (AFM) image is shown on the right. The symbols $\#$ and \parallel indicate where the PMMA layer was cross-linked ($\#$) and left pristine (\parallel), respectively.

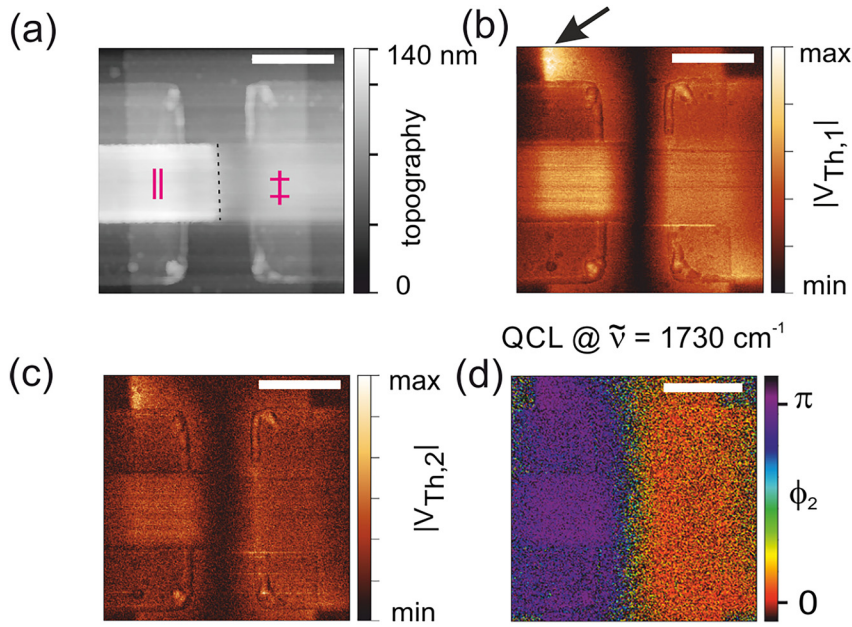


Figure 2: Thermovoltage maps. The topography of the sample is shown in gray-scale in (a). The symbols \oplus and \parallel indicate where the polymethyl methacrylate (PMMA) layer was cross-linked (\oplus) and left pristine (\parallel), respectively. The border between the two regions is marked by the dashed line. The other three maps (b)–(d) show the demodulated thermovoltage amplitude and phase, $|V_{Th,1,2}|$ and ϕ_2 , respectively. Subscripts 1 and 2 refer to the fundamental and second harmonic of the excitation frequency. The arrow indicates the generation of thermovoltage outside the Pt contact increasing toward the left hand edge. This represents a homogeneous layer configuration, considered below in Figure 3. The scale bar represents 1 μm .

the 20 nm thick Pt layer contacting the multi-layered CoFeB/Pt bar, where the structure forms essentially a vertical thermocouple of two materials of different Seebeck coefficients.

Because of the phase sensitive lock-in detection, the phase ϕ_2 of the demodulated thermovoltage jumps from π

to 0 when the tip moves from left to right, as seen in Figure 2(d). The thermovoltage map recorded at $n = 2$ shows qualitatively the same features but sharper edges compared to the thermovoltage demodulated at $n = 1$. This can be understood similarly to the case when the scattered light is detected in s-SNOM, where spatial resolution seems

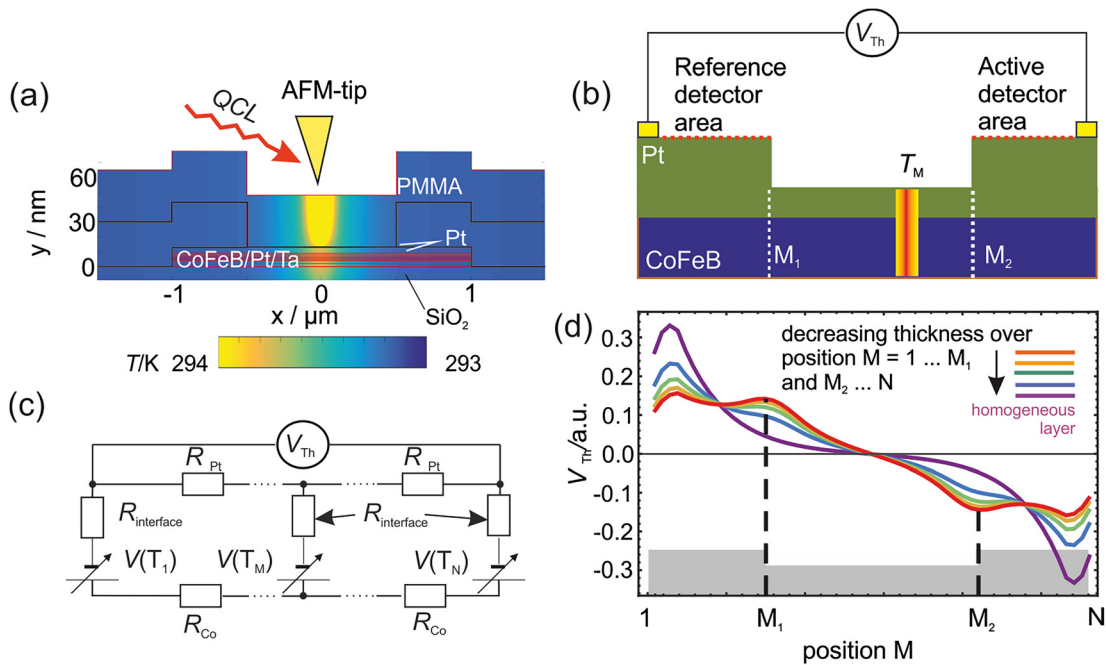


Figure 3: Device operation.

(a) Cross-section of the device superimposed by the numerically determined temperature distribution. (b) Simplified cross-section, consisting of the two layers, Pt and CoFeB, having different Seebeck coefficients, and used for the circuit diagram in (c). (d) Numerically determined thermovoltage for the circuit diagram in (c) for varying layer thicknesses of the active detector area.

to be enhanced at higher order demodulation [21]. Signals demodulated at higher harmonics transfer information at higher spatial frequencies. This indicates that the near-field can drive electronic currents inside the CoFeB/Pt bar which are dissipated and lead to a thermovoltage.

The generated thermovoltage is increased whenever the tip resides above the Pt contact covered with pristine PMMA (marked with || in Figure 1) since it is only there that energy can be effectively transformed into heat in the polymer via near-field mediated absorption of the incoming radiation. However, when the tip is located over the cross-linked PMMA (marked with ‡ in Figure 1), the contrast is almost identical to the thermovoltage induced on the bare contact. This is due to the decreased absorption cross-section of cross-linked PMMA at 1730 cm^{-1} compared to the pristine one (see Supplementary material). Thus, the tip acts as a local heat source being switched on and off depending on the materials ability to absorb light of a certain frequency.

A thermovoltage is also generated on the multilayer slab itself, outside the Pt contact, indicated by the arrow. Over the multilayer slab the thermovoltage increases toward the edge, compared to a more homogeneous distribution over the Pt contact. This qualitative difference in thermovoltage distribution near the multilayer slab edge compared to the Pt contact can be understood by considering the local circular currents of opposite orientation near the localized heat source. A simple qualitative circuit model, shown in Figure 3, aims to illustrate this interplay between the circular currents. It discretizes the cross-section shown in Figure 3(a) into a number of networks. The temperature profile shown was numerically solved by the finite element method (FEM) [22]. The absorption of the nanofocused IR radiation within the PMMA layer is accounted for by a Gaussian hotspot with a lateral standard deviation of 10 nm which vertically decays exponentially with a decay rate of 0.1 nm^{-1} . The thermoelectric device is modeled as described in Figure 1(a) with thermal conductivity for PMMA (0.2 W/mK) [23], CoFeB (87 W/mK) [24], Pt (71.6 W/mK) [25], Ta (57.5 W/mK) [25], and SiO_2 (1.2 W/mK) [26] with only the lower face of the SiO_2 layer being kept at room temperature (293.15 K). As a consequence, the energy dissipated in the PMMA distributes in the device forming a temperature gradient underneath the tip. Due to the large thermal conductivity of the metal layers compared to PMMA, the lateral temperature gradient is an order of magnitude larger than the vertical one in the CoFeB/Pt layer.

Figure 3(b) shows a simplified cross-section of the two metals forming the thermocouple. The extension to the complete multistack will lead to similar results, as shown in

the Supplementary material. The corresponding circuit diagram is provided in Figure 3(c). The circuit consists of several discrete elements, where R_{Pt} , R_{Co} , $R_{\text{interface}}$ and $V(T_n)$ describe the resistances within the Pt layer, the CoFeB layer, across the Pt–CoFeB interface, and the thermovoltage generated at the discrete position n , respectively. In this example, the Pt contacts range over elements $1 \dots M_1$ and $M_2 \dots N$. The AFM tip is located at position M , elevating the temperature T_M by means of near-field interaction between tip and surface. In this simple model, we assume a nonzero lateral temperature gradient along the interface and neglect the vertical temperature gradient.

Heating the symmetric circuit in the center, i.e., with $M_1 = M_2$ and $M = N/2$, would produce an equal amount of circular currents with opposite orientation, resulting in a net zero voltage drop V_{Th} across the N resistors R_{Pt} . Heating away from the center will result in a nonzero V_{Th} . The diagram in Figure 3(d) illustrates the effect of varying thickness of the Pt contact layer. We calculated V_{Th} for illustrative purpose for a specific selection of $R_{\text{interface}}/R_{\text{Pt}} = 50$ and $R_{\text{Co}}/R_{\text{Pt}} = 2$ from the circuit network ($N = 55$, $M_1 = 15$, $M_2 = 40$) in Figure 3(c) as shown in Figure 3(d). The temperature distribution is assumed to be Gaussian with a full width at half maximum (FWHM) of six elements. As the layer thickness is increased the resistance of the Pt-film R_{Pt} decreases over this region. In Figure 3(d) we let R_{Pt} vary as $R_{\text{Pt}} = \frac{1}{4}$ (violet) \dots $\frac{1}{5}$ (red) over the contact. The thermovoltage distribution for thick Pt contacts is relatively homogeneous over the contact area (red). In the center of the device between the two Pt electrodes the signal is zero. Therefore, the region of interest is over the Pt electrodes themselves, in agreement with the measurements in Figure 2. This is where the molecular finger printing can be seen. A vanishing voltage in the center of the device is a consequence of its symmetry.

As the Pt contacts become thinner the thermovoltage becomes localized near the edge (violet). The localization is also observed in the measurement in Figure 2(b) as indicated by the arrow. It lies outside the Pt contact, i.e., there is no variation in the Pt layer thickness. Hence a contact layer of optimal thickness may enlarge the detector area leading to a homogeneous signal distribution.

4 Thermoelectric nanospectroscopy

The scheme may now readily be extended to nanospectroscopy. We recorded a sequence of thermovoltage maps at different incident laser frequencies covering the carbonyl stretching mode $\nu(\text{C}=\text{O})$ of PMMA (Figure 4).

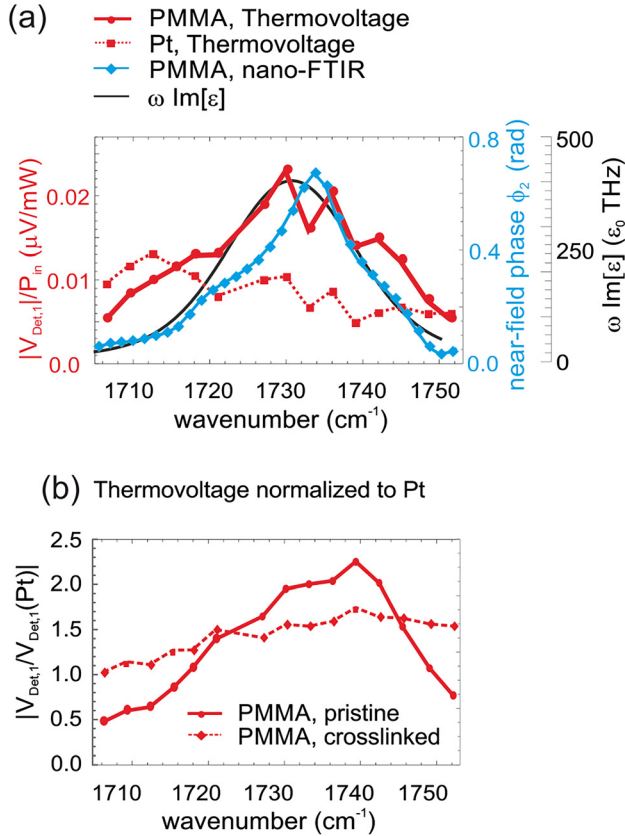


Figure 4: Thermoelectric nanospectroscopy.

(a) Thermovoltage $V_{\text{Det},1}$ (red) of pristine polymethyl methacrylate (PMMA) (solid) and Pt (dotted) as function of laser excitation wavenumber, normalized by the laser power P_{in} . Comparison to $\omega \text{Im} \epsilon$ with ϵ taken from a study by Tsuda et al. [27] (black) and near-field phase ϕ_2 (blue) recorded by an optical scattering-type scanning near-field optical microscopy (s-SNOM). (b) Thermovoltage spectrum of pristine (solid) and cross-linked (dashed) PMMA, normalized to Pt.

Figure 4(a) shows the extracted thermovoltage as function of the wavenumber on the pristine PMMA (solid red) and the Pt contact on the CoFeB slab (dotted red), both normalized to the incident power. The thermovoltage of pristine PMMA follows closely $P_h \propto \omega \text{Im} \epsilon$ (Eq. (1)) shown in black, with $\epsilon(\omega)$ for PMMA taken from a study by Tsuda et al. [27]. We conclude that the thermovoltage, $V_{\text{Det},1}$, corresponds to the heat, P_h , generated by absorbing the IR radiation mainly in the PMMA layer. Owing to its flat spectral response, the thermovoltage on the Pt contact (red, dotted) shows no distinctive spectral features in this region.

For comparison near-field phase spectrum of the pristine PMMA (blue) is shown, which is the established method for finger printing soft material using the s-SNOM [28]. The near-field phase, ϕ_2 , has been measured by combining the s-SNOM with an interferometer and using broadband IR radiation provided by an electron storage

ring, identical to the nano-Fourier-transform infrared (nano-FTIR) setup in Hermann et al. [29]. In the nano-FTIR setup, an *external* detector measures the light scattered from the AFM tip. Here the detector signal has been demodulated at the second harmonic of the tip modulation frequency, Ω , from which the near-field phase, ϕ_2 , was obtained. The maximum of ϕ_2 is slightly shifted to higher wavenumbers compared to the maximum of the absorbed IR radiation. This shift between far-field absorbance and near-field phase has been discussed in detail in a study by Mastel et al. [30].

Figure 4(b) compares the spectra of pristine (solid) and cross-linked (dashed) PMMA, normalized to the signal of Pt on the same map. The cross-linked PMMA shows a flat response, as expected from the thermovoltage maps of Figure 2. A shift to higher thermovoltage values can be observed, which may be due to the lower thickness of the cross-linked PMMA. The near-field power is mainly absorbed near the surface and converted into heat. The smaller distance of the heated surface to the Pt contact may lead then to a higher thermovoltage signal. In addition the spectra are less noisy than in Figure 2(a). The reason may be that the change of laser frequency is accompanied by a change in beam direction. The optimization procedure prior to each thermovoltage map may lead to residual deviations. When normalizing on a signal from the same thermovoltage map, in this case from the Pt region, then these deviations will not show up.

From the same data set we extracted a spatio-spectral line scan crossing the material boundary of the pristine PMMA (Figure 5(a)). In Figure 5(b) the absorptive band around 1730 cm⁻¹ is seen which vanishes once the tip leaves the PMMA indicating the performance of our device. Figure 5(c) shows the intensity at 1730 cm⁻¹ of the induced thermovoltage demodulated at $n = 1$ (red line) and the sample's topography. The thermoelectric response correlates well with the topography. The spatial resolution of 200 nm is not as good as typically seen in s-SNOM where 20–30 nm are readily achievable at mid-IR frequencies [31]. However, it is not trivial to estimate the spatial resolution from the present data set since the apparent width of the material boundary or, alternatively, the edge (approx. 60 nm), where pristine PMMA turns into cross-linked, is of similar dimension as the typical apex radii of the used tips (approx. 30 nm). In principle, the spatial resolution should be comparable to s-SNOM, i.e., dependent on the apex radius. The corresponding field distribution determines the interaction volume, responsible for both, the material dependent scattered and dissipated radiation. To elaborate the theoretically achievable spatial resolution we ran a FEM simulation discussed in the Supplementary material.

For best approximation of the spatial resolution a sample is required which changes its material contrast by means of IR absorption bands without a change in topography to exclude any cross-talk.

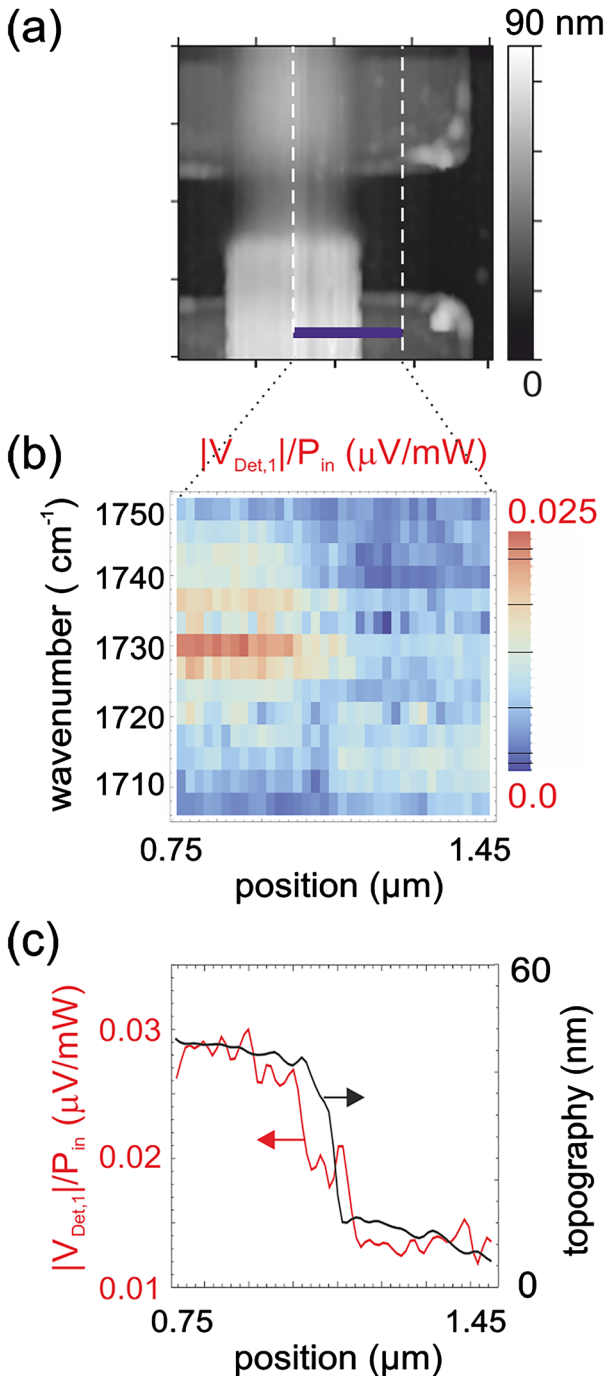


Figure 5: Spectral line scan.

(a) Atomic force microscopy (AFM) topography of the device, showing the location of the line scan. (b) Line scan of the spectrally resolved thermovoltage when scanning across the PMMA-edge. (c) Thermovoltage for laser tuned to the carbonyl resonance at 1730 cm^{-1} (red) compared to the topographical variation (black).

Unlike conventional photodetectors our plain device, i.e., without any absorbing sample layer present should ideally show no response. Nevertheless, the sample layer together with the device can be regarded as a photodetector at the samples resonance frequency. As a measure of sensitivity, we estimate for this special case the noise equivalent power $NEP = S_n/R$ of our platform from the noise spectral density $S_n = 10^{-9}\text{ V Hz}^{-1/2}$ and the responsivity R . Assuming that the excitation area is determined by the tip radius of approximately 25 nm and with an estimated power density close to the tip of 0.01 GW/m^2 [12], we obtain $R = 0.7\text{ V/W}$ at 1730 cm^{-1} , resulting in $NEP = 1.4 \times 10^{-9}\text{ W Hz}^{-1/2}$. Our platform shows a comparable performance to conventional non-cooled photovoltaic detectors and also to recently developed nanophotothermoelectric platforms based on single-layer graphene [32].

5 Conclusion

In this work, we presented a new on-chip detection platform capable of molecular finger printing and nanoscale spatially resolved thermoelectric detection of soft materials. It combines thermoelectric and spectroscopic films in a hybrid device, allowing nanospectroscopy of materials that do not show thermoelectricity themselves. This flexibility allows to enhance the sensitivity by employing tailor-made thermoelectric materials with large differences in the Seebeck coefficient. Alternatively, recently explored materials exhibiting a strong anomalous Nernst effect may be considered, adding contributions from magneto-thermal effects to the detection signal [33]. In addition, one can optimize power dissipation into the film to be detected by tip-enhanced fields without the need to simultaneously consider the complicated re-radiation and detection process. The technique was demonstrated on a nanopatterned hybrid architecture consisting of an insulating polymer and a conducting metal heterostructure. The thermovoltage measured at the heterostructure revealed spectroscopic information of the film covering the heterostructure. While our device has an active area of only $\approx 2\text{ }\mu\text{m}^2$, it may be – in principle – extended to a larger total detection area by connecting many of these microstructures into an array. The need for external electrical contacts may be further relaxed by using a contactless inductive current sensing scheme or by means of nitrogen vacancy centers, which have already been implemented in AFMs [34]. The proof-of-principle presented in this work may be exploited for on-chip high-resolution thermoelectric detection of soft materials at the nanoscale.

Acknowledgments: The authors would like to thank Zbynek Soban for fabricating the Anomalous Nernst Effect (ANE) device shown in the Supplementary material. DV, JW and HS acknowledge funding from the ERC Synergy Grant SC2 (Grant No. 610115). GS acknowledges postdoctoral fellowship support from The Leverhulme Trust (Early Career Fellowship supported by the Isaac Newton Trust). EP and JH are grateful for funding by the DFG through project HE 2063/5-1. BK and GU received funding within the JRP “MetVBadBugs” and “RaChy” from the EMPIR programme cofinanced by the Participating States and from the European Union’s Horizon 2020 Research and Innovation Programme.

Author contribution: E.P., B.K., J.W. and D.V conceived the study, planned and prepared the measurements, which G.U., E.P., A.H., B.K., J.W., and D.V. carried out. G.U., E.P., B.K., J.W. and D.V. wrote the paper. J-W.L., O.Z., G.S. contributed to the sample preparation. All authors discussed the results and contributed to the manuscript.

Research funding: DV, JW and HS acknowledge funding from the ERC Synergy Grant SC2 (Grant No. 610115). GS acknowledges postdoctoral fellowship support from The Leverhulme Trust (Early Career Fellowship supported by the Isaac Newton Trust). EP and JH are grateful for funding by the DFG through project HE 2063/5-1. BK and GU received funding within the JRP “MetVBadBugs” and “RaChy” from the EMPIR programme cofinanced by the Participating States and from the European Union’s Horizon 2020 Research and Innovation Programme.

Conflict of interest statement: The authors declare no conflicts of interest regarding this article.

References

- [1] R. M. Stöckle, Y. D. Suh, V. Deckert, and R. Zenobi, “Nanoscale chemical analysis by tip-enhanced Raman spectroscopy,” *Chem. Phys. Lett.*, vol. 318, no. 1, pp. 131–136, 2000.
- [2] M. V. Balois, N. Hayazawa, C. Chen, et al., “Development of tip-enhanced Raman spectroscopy based on a scanning tunneling microscope in a controlled ambient environment,” *Jpn. J. Appl. Phys.*, vol. 58, SI, p. SI0801, Jun. 2019.
- [3] B. Knoll and F. Keilmann, “Near-field probing of vibrational absorption for chemical microscopy,” *Nature*, vol. 399, May, p. 134, 1999.
- [4] A. Hartschuh, “Tip-enhanced near-field optical microscopy,” *Angew. Chem. Int. Ed.*, vol. 47, no. 43, pp. 8178–8191, 2008.
- [5] F. Keilmann and R. Hillenbrand, “Near-field nanoscopy by elastic light scattering from a tip,” in *Nano-Optics and Near-Field Optical Microscopy*, A. Zayats and D. Richard, Eds., Boston, London, Artech House, 2009, pp. 235–265.
- [6] A. Dazzi, R. Prazeres, F. Glotin, and J. M. Ortega, “Local infrared microspectroscopy with subwavelength spatial resolution with an atomic force microscope tip used as a photothermal sensor,” *Optic Lett.*, vol. 30, no. 18, pp. 2388–2390, 2005.
- [7] I. Rajapaksa, K. Uenal, and H. K. Wickramasinghe, “Image force microscopy of molecular resonance: a microscope principle,” *Appl. Phys. Lett.*, vol. 97, no. 7, p. 73121, 2010.
- [8] R. A. Mardick, W. Morrison, D. Nowak, T. R. Albrecht, J. Jahng, and S. Park, “Photoinduced force microscopy: A technique for hyperspectral nanochemical mapping,” *Jpn. J. Appl. Phys.*, vol. 56, no. 8S1, p. 08LA04, Jul. 2017.
- [9] A. Woessner, P. Alonso-González, M. B. Lundeberg, et al., “Near-field photocurrent nanoscopy on bare and encapsulated graphene,” *Nat. Commun.*, vol. 7, p. 10783, 2016.
- [10] M. B. Lundeberg, Y. Gao, A. Woessner, et al., “Thermoelectric detection and imaging of propagating graphene plasmons,” *Nat. Mater.*, vol. 16, no. 2, pp. 204–207, Feb. 2017.
- [11] P. Alonso-González, A. Y. Nikitin, Y. Gao, et al., “Acoustic terahertz graphene plasmons revealed by photocurrent nanoscopy,” *Nat. Nanotechnol.*, vol. 12, no. 1, pp. 31–35, Jan. 2017.
- [12] E. Pfizner, X. Hu, H. W. Schumacher, et al., “Near-field magneto-caloritronic nanoscopy on ferromagnetic nanostructures,” *AIP Adv.*, vol. 8, p. 125329, 2018.
- [13] S. S. Sunku, A. S. McLeod, T. Stauber, et al., “Nano-photocurrent mapping of local electronic structure in twisted bilayer graphene,” *Nano Lett.*, vol. 20, no. 5, pp. 2958–2964, May 2020.
- [14] B. Kästner, C. M. Johnson, P. Hermann, et al., “Infrared nanospectroscopy of phospholipid and surfactin monolayer domains,” *ACS Omega*, vol. 3, no. 4, pp. 4141–4147, Apr. 2018.
- [15] A. Woessner, R. Parret, D. Davydovskaya, et al., “Electrical detection of hyperbolic phonon-polaritons in heterostructures of graphene and boron nitride,” *npj 2D Mater. Appl.*, vol. 1, no. 1, p. 25, Dec. 2017.
- [16] L. D. Landau, E. M. Lifshitz, and P. Pitaevskii, *Electrodynamics of Continuous Media*, Amsterdam, Elsevier Corporation, 1960.
- [17] S. J. Orfanidis. *Electromagnetic Waves and Antennas*, Rutgers University, 2016. <http://www.ece.rutgers.edu/~orfanidi/ewa/ch01.pdf>.
- [18] J. M. Bartell, D. H. Ngai, Z. Leng, and G. D. Fuchs, “Towards a tabletop microscope for nanoscale magnetic imaging using picosecond thermal gradients,” *Nat. Commun.*, vol. 6, p. 8460, 2015.
- [19] J. C. Karsch, J. M. Bartell, and G. D. Fuchs, “Near-field coupling of gold plasmonic antennas for sub-100 nm magneto-thermal microscopy,” *APL Photonics*, vol. 2, no. 8, p. 086103, 2017.
- [20] T. Tada and T. Kanayama, “Fabrication of silicon nanostructures with a poly(methylmethacrylate) single-layer process,” *J. Vac. Sci. Technol. B – Microelect. Nanometer Struct. Process. Meas. Phenom.*, vol. 13, p. 2801, 1995.
- [21] S. Mastel, A. A. Govyadinov, C. Maissen, A. Chuvilin, A. Berger, and R. Hillenbrand, “Understanding the image contrast of material boundaries in IR nanoscopy reaching 5 nm spatial resolution,” *ACS Photonics*, vol. 5, no. 8, pp. 3372–3378, 2018.
- [22] F. Hecht, “New development in freefem++,” *J. Numer. Math.*, vol. 20, nos 3–4, pp. 251–265, 2012.
- [23] M. J. Assael, S. Botsios, K. Gialou, and I. N. Metaxa, “Thermal conductivity of polymethyl methacrylate (PMMA) and borosilicate crown glass BK7,” *Int. J. Thermophys.*, vol. 26, no. 5, pp. 1595–1605, 2005.
- [24] T. Huebner, A. Boehnke, U. Martens, et al., “Comparison of laser-induced and intrinsic tunnel magneto-Seebeck effect in CoFeB/

- MgAl₂O₄ and CoFeB/MgO magnetic tunnel junctions,” *Phys. Rev. B*, vol. 93, no. 22, pp. 1–6, 2016.
- [25] C. Y. Ho, R. W. Powell, and P. E. Liley, “Thermal conductivity of the elements,” *J. Phys. Chem. Ref. Data*, vol. 1, no. 2, pp. 279–421, Apr. 1972.
- [26] S. Callard, G. Tallarida, A. Borghesi, and L. Zanotti, “Thermal conductivity of SiO₂ films by scanning thermal microscopy,” *J. Non-Cryst. Solids*, vol. 245, nos 1–3, pp. 203–209, Apr. 1999.
- [27] S. Tsuda, S. Yamaguchi, Y. Kanamori, and H. Yugami, “Spectral and angular shaping of infrared radiation in a polymer resonator with molecular vibrational modes,” *Optic Express*, vol. 26, no. 6, p. 6899, 2018.
- [28] E. A. Muller, B. Pollard, and M. B. Raschke, “Infrared chemical nano-imaging: accessing structure, coupling, and dynamics on molecular length scales,” *J. Phys. Chem. Lett.*, vol. 6, no. 7, pp. 1275–1284, Apr. 2015.
- [29] P. Hermann, B. Kästner, A. Hoehl, et al., “Enhancing the sensitivity of nano-FTIR spectroscopy,” *Optic Express*, vol. 25, no. 14, pp. 16574–16588, Jul. 2017.
- [30] S. Mastel, A. A. Govyadinov, T. V. A. G. de Oliveira, I. Amenabar, and R. Hillenbrand, “Nanoscale-resolved chemical identification of thin organic films using infrared near-field spectroscopy and standard Fourier transform infrared references,” *Appl. Phys. Lett.*, vol. 106, no. 2, p. 023113, Jan. 2015.
- [31] F. Huth, A. Govyadinov, S. Amarie, W. Nuansing, F. Keilmann, and R. Hillenbrand, “Nano-FTIR absorption spectroscopy of molecular fingerprints at 20 nm spatial resolution,” *Nano Lett.*, vol. 12, no. 8, pp. 3973–3978, Aug. 2012.
- [32] Q. Guo, R. Yu, C. Li, et al., “Efficient electrical detection of mid-infrared graphene plasmons at room temperature,” *Nat. Mater.*, vol. 17, no. 11, pp. 986–992, 2018.
- [33] H. Reichlova, T. Janda, J. Godinho, et al., “Imaging and writing magnetic domains in the non-collinear antiferromagnet Mn₃Sn,” *Nat. Commun.*, vol. 10, no. 1, 2019, <https://doi.org/10.1038/s41467-019-13391-z>.
- [34] K. Chang, A. Eichler, J. Rhensius, L. Lorenzelli, and C. L. Degen, “Nanoscale imaging of current density with a single-spin magnetometer,” *Nano Lett.*, vol. 17, no. 4, pp. 2367–2373, 2017.

Supplementary Material: The online version of this article offers supplementary material (<https://doi.org/10.1515/nanoph-2020-0316>).